# Chapter 4

# Two-dimensional (2D) $MoS_2$ Nanosheets on $MoNi_4/MoO_2$ Nanorods for Hydrogen Evolution Reaction

## 4.1 Introduction

This chapter discussed the development of $MoS_2$:$MoNi_4$/$MoO_2$ nanohybrids and their structural characterizations such as (XRD, FESEM, TEM/HRTEM, and XPS) followed by application in hydrogen evolution reaction (HER).

In the past few decades, various combinations of materials, including metals, metal alloys [1], metals modified with transition metal (mainly Ni or Mo-based) carbides [2], chalcogenides [3], nitrides [4], phosphides[5], and heteroatom doped carbon nanostructures[6, 7], have been utilized to catalyze the conversion of $H_3O^+$ (acid) and $H_2O$ (alkaline) to $H_2$ [8, 9]. Among these materials, transition metal alloys are the key-emerging materials having good electrical conductivity, higher electrocatalytic activities, high corrosion resistance, and good stability. These transition metal compounds are earth-abundant, eco-friendly, and low-cost materials with significantly higher catalytic activities for HER reaction. In specific, hydrogen binding free energies ($\Delta G_H$) could be regulated on the surface by alloying Ni with Mo due to modification of d-band electron density states, thus facilitate the faster adsorption/desorption of hydrogen molecules [8, 10]. In this regard, Mo and Ni-based alloys showed high promises for HER electrocatalysts, and still, there are many rooms available for improving the performance of state-of-the-art Pt-free catalysts for HER [11]. In these materials, Mo atoms exhibit superior adsorption properties towards hydrogen, while Ni atoms are broadly recognized as excellent water dissociation centers [12, 13]. Therefore, Ni–Mo-based alloy electrocatalysts ($Mo_xNi_y$) can be promising candidates to speed up the sluggish HER kinetics under alkaline conditions and effectively reduce the Volmer-step energy barrier [11]. However, under alkaline conditions, the Volmer step on these Pt-free electrocatalysts still appears to be slower than Pt catalyst and hence showed lower activity for HER reactions [1, 14]. Strikingly, over decades of development, it has been observed that only Ni or Mo-based

oxides [11], hydroxides [15], layered double hydroxides [16], phosphides [17], and sulfides [15], exhibits the best efficiencies for water splitting.

Recently $MoS_2$ received considerable attention for HER catalyst as low-cost, high surface area, tunable properties, and abundance. More importantly, different phases of $MoS_2$ (i.e., 2H, 2H′, and 3R, which exhibit semiconducting, whereas 1T′, and 1T″ show metallic) and their structures and electronic properties have shown promising as a catalyst for HER [18]. The rich active sites on the nanosheets' exposed edges are responsible for this high HER activity, as reported previously [19]. Also, various factors such as expanded interlayer spacing, the basal plane activation, increased defects, disorder engineering, and doping of heteroatoms are responsible for further enhancing the HER catalytic performance of $MoS_2$ nanosheets apart from increasing the active sites on edges [20-26]. Furthermore, it is quite well-known that in the traditional hydrodesulfurization (HDS) process, the S content in $MoS_2$ also plays a vital role in HER [27, 28]. $MoS_2$ containing unsaturated sulfur atoms on the surface can engage the discharge reaction and rapidly form S−H bonds, which leads to hydrogen formation eventually. For example, Hu's group reported that amorphous $MoS_3$ particles, which contain catalytically active $S_2^{2-}$ ligands, show superior catalytic activity towards HER [29]. Although significant progress has been achieved so far, the catalytic performance of $MoS_2$ is still lacking compared to the Pt-based catalysts. For further improvements in the HER activity of 2D $MoS_2$, various architectures have been proposed by introducing 2D $MoS_2$ nanosheets on the surface of conductive substrates, especially carbonaceous materials that can provide a conductive channel for semiconducting $MoS_2$ nanosheets. The improved HER catalytic performance has been demonstrated by depositing $MoS_2$ nanosheets on various conductive membranes, including graphene [30], carbon nanotubes [31], hollow carbon sphere [32], carbon cloth [33], etc. In general, a conducting channel may play an important role in smooth transporting electrons through catalytic-

conducting interfaces, which could effectively improve such synergistic nanostructures' catalytic activity. To this point, employing a catalytically active conducting channel with 2D $MoS_2$ would have exciting possibilities for enhancing the HER performance of such 2D-1D junction-based nano-heterostructures.

In this work, we report the synthesis of high-surface-area novel nano-scale hybrid material by depositing 2D flaky $MoS_2$ nanosheets onto $MoNi_4/MoO_2$ nanorods using a facile, one-pot hydrothermal synthesis technique described detail in chapter 2 (section 2.1.7). We use different characterization techniques, including X-ray diffraction (XRD), field emission scanning electron microscopy (FESEM), transmission electron microscopy (TEM)/ high-resolution transmission electron microscopy (HRTEM), selected area electron diffraction (SAED), and X-ray photoelectron spectroscopy (XPS), to demonstrate the structure, phases, and morphologies of the as-grown nanohybrid materials. Furthermore, we did various electrochemical measurements to investigate the electrocatalytic performances of the $MoS_2$:$MoNi_4/MoO_2$ nanohybrid in hydrogen evolution reaction (HER).

**4.2 Results and discussions**

The as-synthesized 2D-$MoS_2$, $MoNi_4/MoO_2$ nanorods, and $MoS_2$:$MoNi_4/MoO_2$ nanohybrid samples were characterized using the grazing incidence X-ray diffraction (XRD) technique for obtaining information regarding the structure and phase formation as shown in Figure 4.1. The diffraction data of 2D-$MoS_2$ (green curve, Figure 4.1a) shows the characteristic (002), (004), (110), (013), and (008) planes at the corresponding peak positions of 14.04˚, 28.76˚, 33.42˚, 39.66˚ 59.02˚, respectively. The $MoS_2$ peaks and peak positions suggest the formation of 2H-$MoS_2$ (JCPDS No. 98-001-8125) via a low-temperature hydrothermal process. Similarly, we obtained the XRD data of $MoNi_4/MoO_2$ nanorods, as shown in Figure 4.1a (gray curve) and Figure 4.2b. The XRD data of $MoNi_4/MoO_2$ nanorods showed the primary

peaks at 31.0˚, 43.92˚, 51.16˚, 54.40˚, 56.24˚, and 75.32˚, which correspond to the (020), (121), (002), (031), (112), and (512) crystal planes of $MoNi_4$ (JCPDS No. 98-007-4658). A few XRD peaks were observed at 26.22˚, 36.72˚, 49.98˚, 53.17˚, and 63.42˚, and those peaks correspond to the (110), $(11\bar{2})$, $(22\bar{1})$, (121), and $(22\bar{3})$ crystal planes of metallic $MoO_2$ (JCPDS No. 98-001-7724) [11, 34, 35]. The XRD of $MoS_2$:$MoNi_4/MoO_2$ nanohybrid sample shows the characteristic peaks of both 2H-$MoS_2$ and $MoNi_4/MoO_2$ simultaneously, as depicted in Figure 4.1 (black curve), indicating the growth of 2H-$MoS_2$ on the surface of $MoNi_4/MoO_2$ nanorods. It should be mentioned here that no other impurity peaks are found in the hybrid material's XRD data, which further implies that the successful formation of the hybrid material occurred with 2H-$MoS_2$ flakes on $MoNi_4/MoO_2$ nanorods.

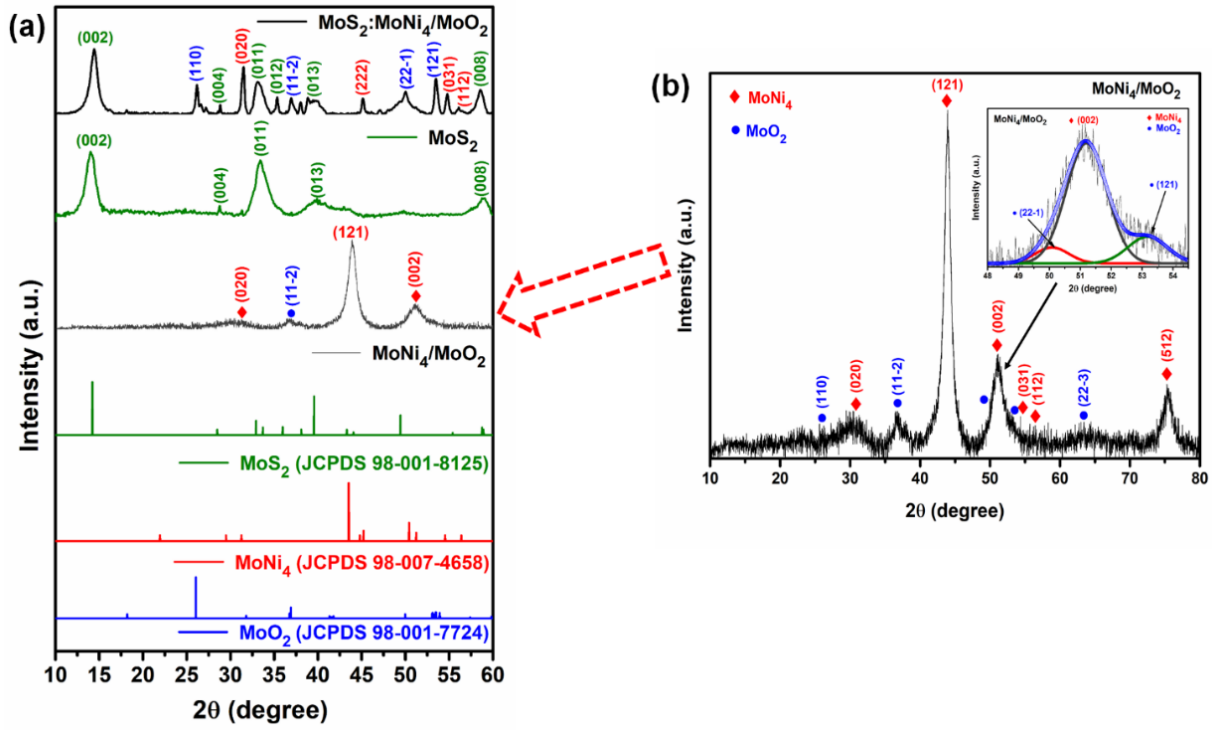


***Figure 4.1:*** *Shows (a) Comparative XRD patterns of 2D $MoS_2$, $MoNi_4/MoO_2$ nanorod, and $MoS_2$:$MoNi_4/MoO_2$ nanohybrids; (b) XRD patterns of $MoNi_4/MoO_2$.*

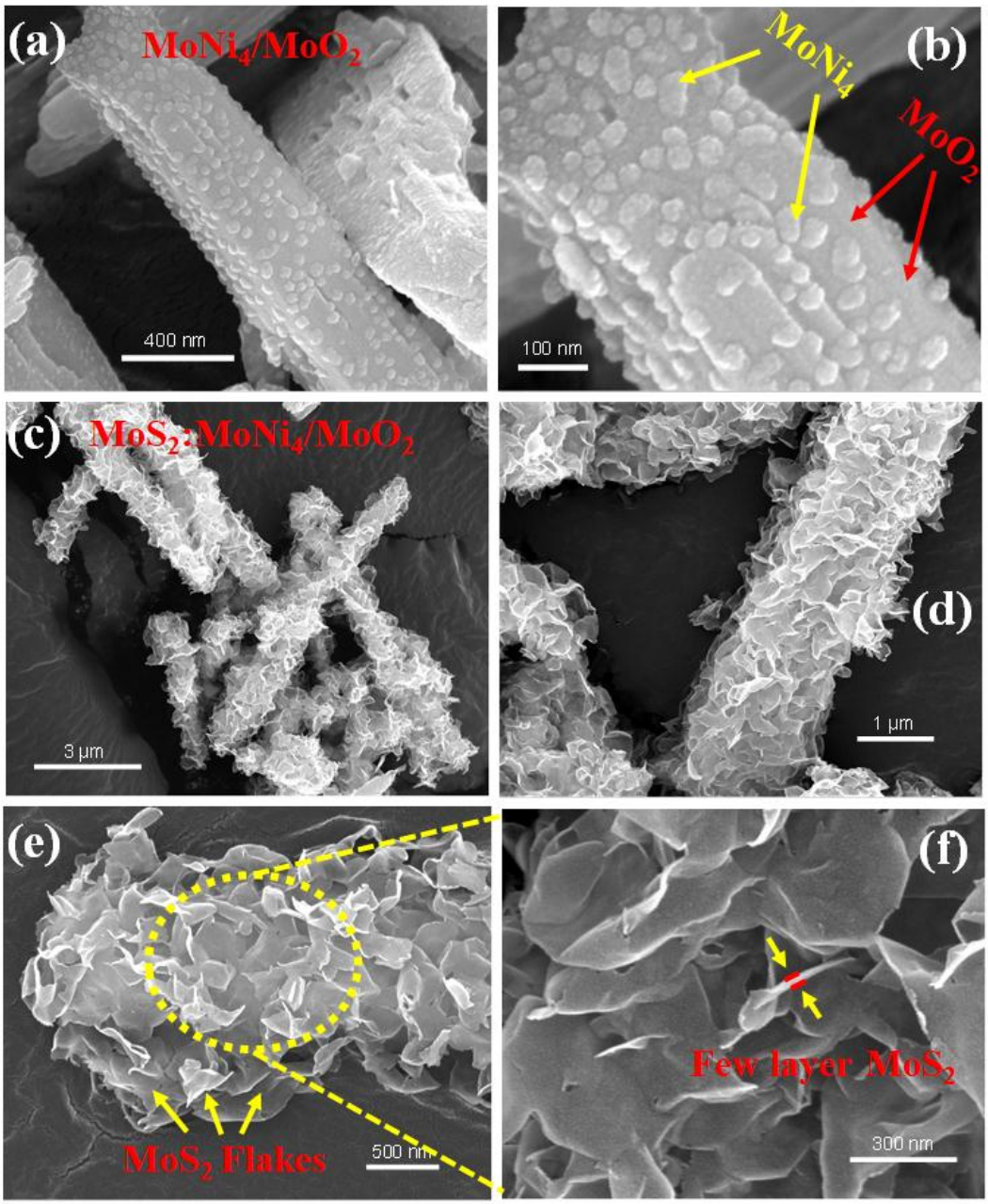


***Figure 4.2:*** *Shows the FESEM images of (a) $MoNi_4/MoO_2$ nanorods; (b) $MoNi_4$ nanocrystals grown on $MoO_2$ nanorods; (c) a few as-grown nanohybrids of $MoS_2$:$MoNi_4/MoO_2$ showing homogeneous coating of $MoS_2$ on $MoNi_4/MoO_2$; (d) & (e) illustrate the nanohybrids with homogeneous coating, large surface area, vertically oriented 2D flake-like of $MoS_2$ grown on $MoNi_4/MoO_2$ nanorods with flake size of ~ 300-500 nm; (f) vertical 2D $MoS_2$ flakes with a thickness of ~ 2-5 nm with sharp edges, which helps in faster electronic transfer, thus, improve the catalytic activity of the nanocomposite.*

The morphology and structure of the as-grown $MoS_2$:$MoNi_4/MoO_2$ nanohybrid materials were characterized using a field emission scanning electron microscope (FESEM), as illustrated in Figure 4.2. For comparison, we have characterized as-synthesized $MoNi_4/MoO_2$ nanorods as shown in Figure 4.2a and Figure 4.2b, which indicate the $MoO_2$ nanorods having a diameter of ~300-500 nm with a length of ~3-5 μm. It is also observed that $MoNi_4$ nanocrystals form on the surface of the $MoO_2$ nanorods, as depicted in Figure 4.2b. The size of the nanocrystals is approximately around 30-50 nm, homogeneously dispersed throughout the surface of the nanorods. Figure 4.2c shows a few segregated $MoS_2$:$MoNi_4/MoO_2$ hybrid-nanostructures with uniformly coated leaf-like flaky $MoS_2$ on the surface of the nanorods. Figure 4.2d and Figure 4.2e delineate vertically grown $MoS_2$ on nanorods with an average flake size of 300-500 nm. It is seen from Figure 4.2e that most of the 2D $MoS_2$ flakes are grown in the vertical direction in a random orientation with a forest-like structure. Thus, these vertically oriented 2D nano-architectures on $MoNi_4/MoO_2$ exhibit a significantly high surface area. Figure 4.2f depict that all the nano-flakes forms flower petals-shaped structures with thickness of ~2-5 nm, which will be explained in the HRTEM section of this chapter. In this regard, it should be mentioned that the nanohybrid architecture is primarily composed of vertically oriented 2D $MoS_2$ onto the $MoO_2$ alloy nanorods, while $MoNi_4$ nanocrystals are at the interface of the both 2D $MoS_2$ and bulk $MoO_2$. It could also be observed that these dense $MoS_2$ flakes are dominated by edges (Figure 4.2e and 4.2f), and all these sharp edges of $MoS_2$ flakes enhance the density of surface-active sites, which provide more electrocatalytically active electron-transfer sites. Consequently, enhancement in the catalytically active edge-plane-like structures will take part in a faster redox reaction via enhancing the charge-transfer process, thus, improving the catalytic activities of the hybrid-nanostructures at room temperature. We have performed the energy dispersive spectroscopy (EDS) in FESEM of $MoNi_4/MoO_2$ nanorods sample, and we obtained the characteristics of

Mo, Ni, and O peaks as shown in Figure 4.3. The elemental distributions of Mo, Ni, and O are obtained from the EDS analysis of $MoNi_4/MoO_2$ as 46.27 (wt.%), 33.90 (wt.%), and 19.83 (wt.%) (Shown in inset of Figure 4.3), respectively.

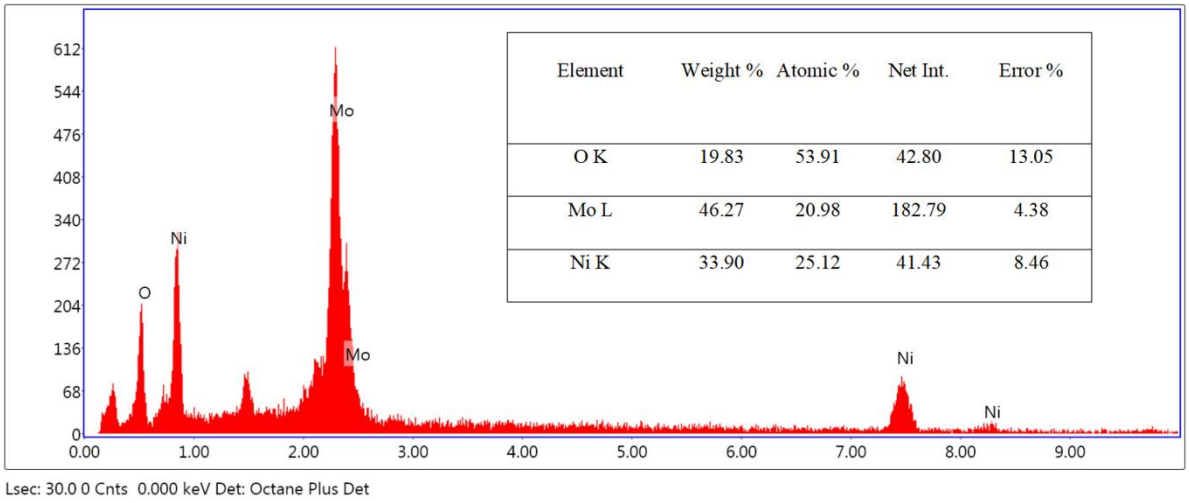


***Figure 4.3:*** *Energy dispersive spectroscopy of $MoNi_4/MoO_2$ nanorods recorded during SEM.*

Figure 4.4 shows the transmission electron micrographs (TEM) and high-resolution transmission electron micrographs (HRTEM) of the as-grown $MoNi_4/MoO_2$ and $MoS_2$:$MoNi_4/MoO_2$ nanohybrid structures. Figures 4.4a and Figure 4.4b demonstrate the TEM images of standalone $MoNi_4/MoO_2$ nanorods, which depict the $MoO_2$ nanorods with dispersed black dots of $MoNi_4$ on the surface. Figure 4.4c shows the SAED pattern of $MoNi_4/MoO_2$ nanorod where (121) and (013) planes correspond to $MoNi_4$ alloys and (112) and (024) correspond to metallic $MoO_2$. Figure 4.4d and Figure 4.4e demonstrate the nanohybrid structure, where 2D $MoS_2$ are grown on $MoNi_4/MoO_2$ nanorods during the hydrothermal process. Figure 4.4d clearly shows that flaky $MoS_2$ is grown throughout the surface of the nanorod. In contrast, Figure 4.4e shows that 2D $MoS_2$ was grown on the tips/edges of the nanorods as well, which manifests the conformal coating of 2D flaky $MoS_2$ on $MoNi_4/MoO_2$ nanorods despite the dimensions and shape, size, and specific area of the nanorod. Figure 4.4f shows the SAED pattern of 2D $MoS_2$ with its characteristic diffraction

planes of (010), (103), and (008) along with $MoNi_4$ (310) and $MoO_2$ (022), suggesting the formation of 2H-$MoS_2$ on $MoNi_4/MoO_2$ nanorods as described in the XRD data (Figure 4.1). The sharp and bright diffraction rings in the SAED pattern suggest that most of the as-grown flaky $MoS_2$ exhibits polycrystalline nature, whereas the presence of multiple spots interprets the growth of fewer single-crystalline $MoS_2$ flakes with smaller sizes.

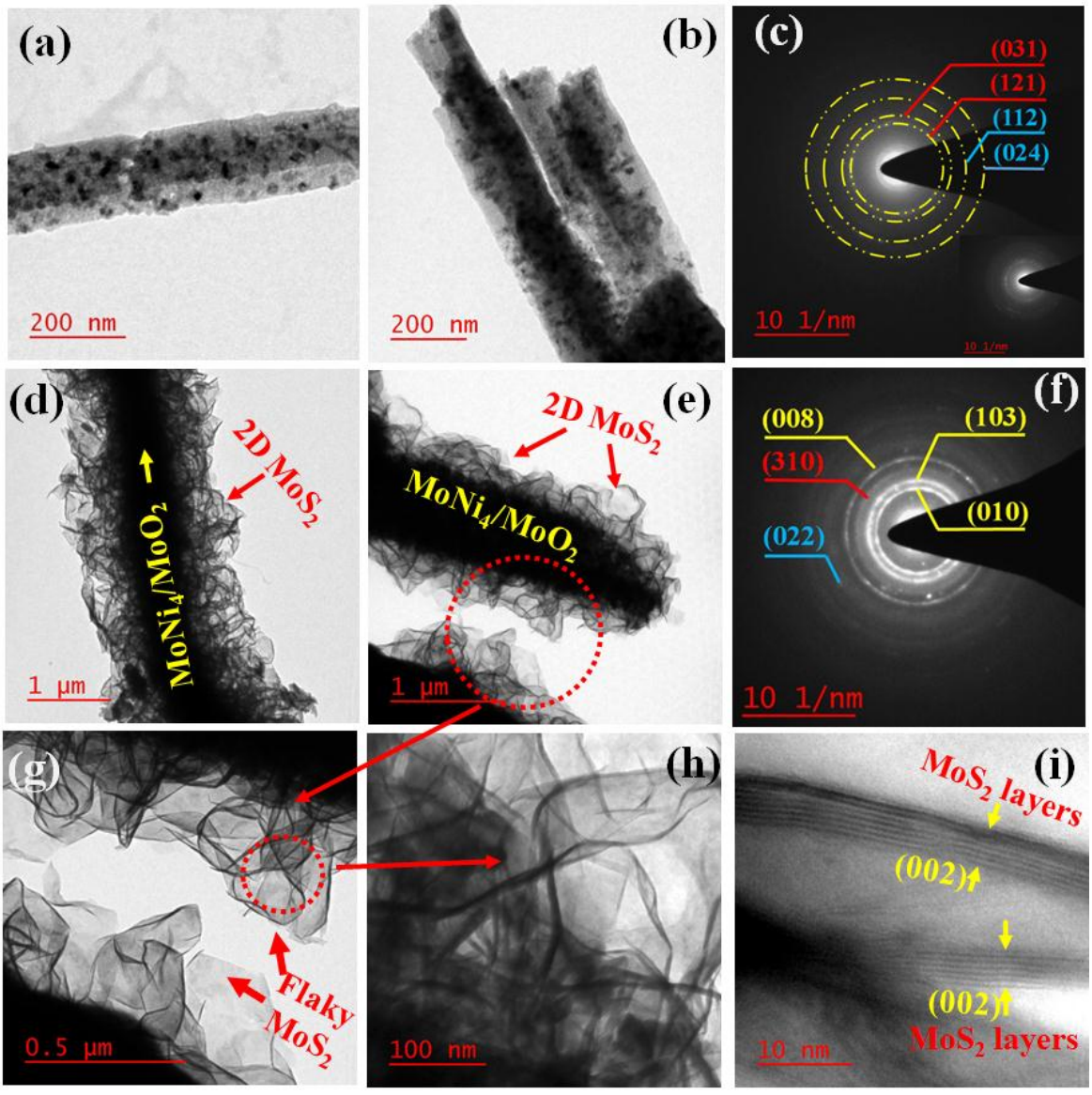


***Figure 4.4:*** *(a, b) Bright field transmission electron micrographs of $MoNi_4/MoO_2$ nanohybrid with different morphologies; (c) SAED pattern of characteristic $MoNi_4/MoO_2$ planes; (d, e, g, h) As-grown 2D $MoS_2$ on $MoNi_4/MoO_2$ nanorods with flaky entangled*

*morphologies; (f) SAED pattern of characteristic $MoS_2$:$MoNi_4/MoO_2$; (i) High-resolution transmission electron micrograph of layered $MoS_2$ with the (002) plane.*

Figure 4.4g and Figure 4.4h shows the flaky morphologies of as-grown $MoS_2$ with entangled forest-like deposition (Figure 4.4g) on the surface of the $MoNi_4/MoO_2$ nanorods. We have optimized the growth time and temperature to obtain the best structure of 2D $MoS_2$ with flakes of ~300−500 nm size and thickness of a few nanometers. Also, it is seen from Figure 4.4h that all 2D $MoS_2$ exhibits sharp edge-plane-like structures, which are electrocatalytically active and play a key role in enhancing the electrocatalytic activities of the nanohybrid structure for the HER, as elaborated further in the electrochemical section of this manuscript. Figure 4.4i shows the HRTEM image of $MoS_2$ flakes where three to four atomically thin monolayers are stacked to each other with an interplanar spacing of 0.64 nm, which is indicative of the (002) plane of $MoS_2$. The as-measured $MoS_2$ flake thickness is ~ 2.5−3.5 nm, which indicates the well-grown two-dimensional structure of $MoS_2$ on transition-metal alloy nanorods. Furthermore, Figure 4.4i shows the continuous layered structure of $MoS_2$, which is quite indicative of highly crystalline 2D $MoS_2$ deposition on $MoNi_4/MoO_2$ nanorods.

Figures 4.5a and Figure 4.5b show the scanning transmission electron microscopy (STEM) images of the synergistic hybrid structure demonstrating the vertically grown and homogeneously coated 2D flaky $MoS_2$ on the bulk nanorod surface, where the sharp tips of surface grown $MoS_2$ are indicative of the edge-plane-like structure with better catalytic activities. We believe that the growth of $MoS_2$ is a self-limiting process, which essentially depends on the temperature, pressure, and concentration of the solution; however, $MoS_2$ flake sizes are merely contingent upon the total time of the hydrothermal process.

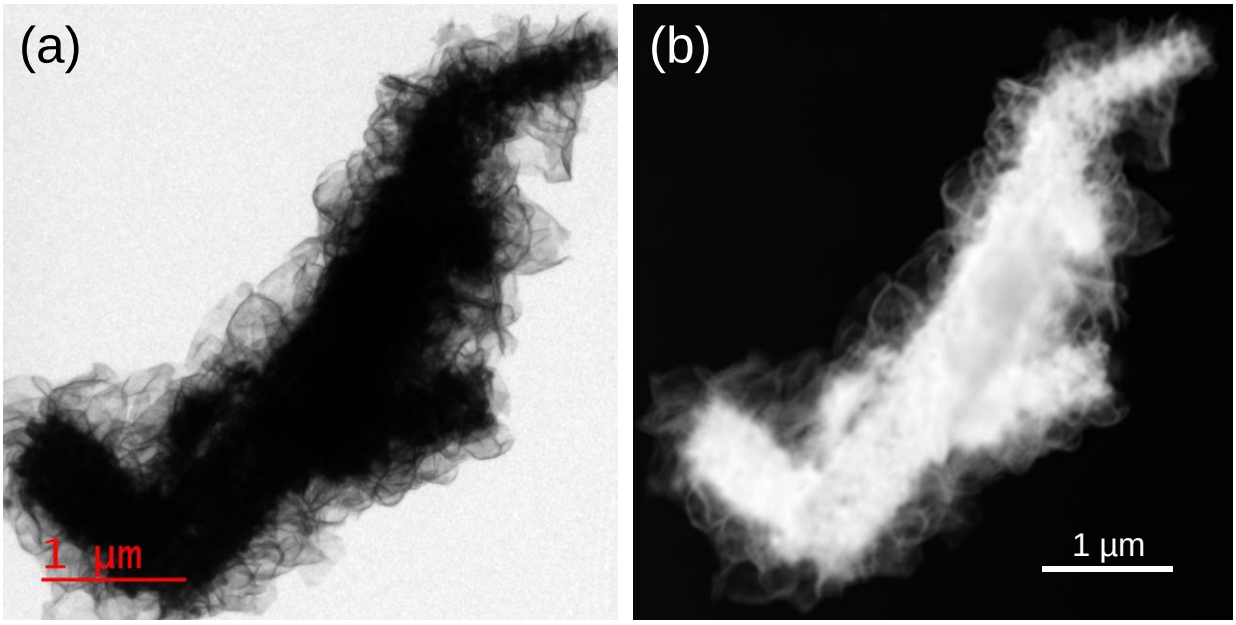


***Figure 4.5:*** *Shows (a) a TEM image of a two-dimensional $MoS_2$ coated: $MoNi_4/MoO_2$ nanohybrid; (b) illustrates the scanning transmission electron microscopy images of a similar structure with clearly visible flaky 2D $MoS_2$ coated onto the transition-metal alloy nanorod.*

Figure 4.6a shows the STEM image, which was used to collect the EDS mapping data as shown in Figure 4.6 (b-f). The as-obtained EDS mapping image is demonstrated in Figure 4.6b, which shows the comprehensive elemental distributions of Mo, Ni, S, and O. Figure 4.6c and Figure 4.6d depict the elemental distribution of Mo and S, respectively, and we believe that most of the trace of Mo and S were appearing from the surface-grown $MoS_2$ of the nanohybrid structure. A clear distribution of Ni and O are found, and they are mostly from the surface of the $MoNi_4/MoO_2$ nanorod, as shown in Figure 4.6e and Figure 4.6f, respectively. The EDS elemental mapping images shown in Figure 4.6 manifest the homogeneous distribution of Mo, S, Ni, and O elements throughout the entire surface of $MoS_2$:$MoNi_4/MoO_2$.

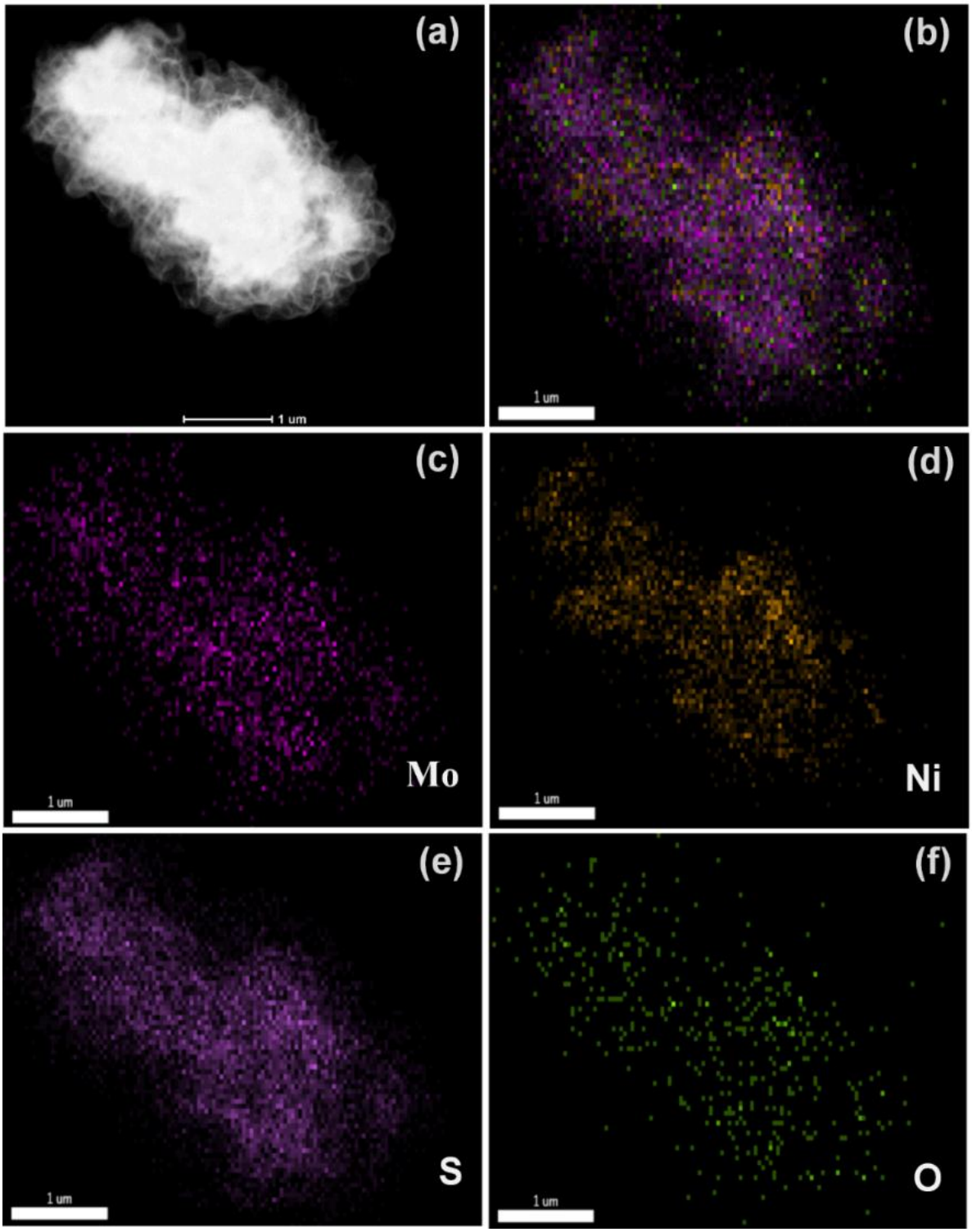


***Figure 4.6**: (a) Shows the STEM image of a $MoS_2$:$MoNi_4$/$MoO_2$ nanohybrid; (b) illustrates the EDS mapping of the nanohybrid showing comprehensive elemental mapping; (c-f) shows the various elemental distributions obtained in EDS mapping, such as, (c) Molybdenum, (d) Sulfur, (e) Nickel, and (f) Oxygen.*

The step-by-step growth mechanism of the $MoS_2$:$MoNi_4/MoO_2$ nanohybrid is schematically demonstrated in Figure 4.7. This mechanism involves dissociation of thiourea, which produces sulfur ions at elevated temperatures/pressures during the hydrothermal process, followed by super saturation of the sulfur ions around the $MoNi_4/MoO_2$ nanorods. Finally, the vertically aligned 2D $MoS_2$ flakes were grown on the nanorod surface after successive nucleation and growth during the growth process.

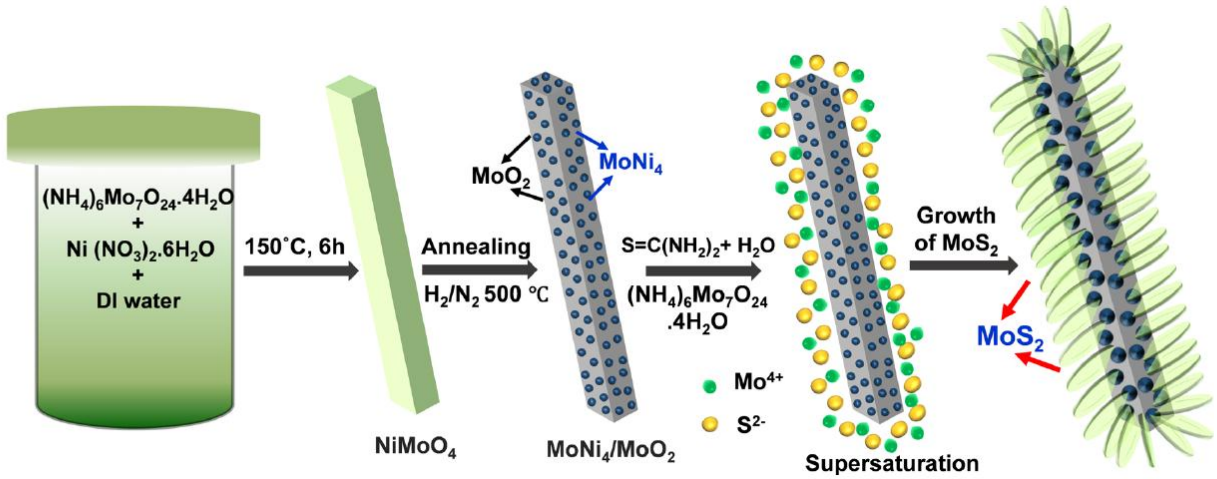


***Figure 4.7:*** *Schematic demonstrating step-by-step mechanism of the growth of 2D $MoS_2$ on the $MoNi_4/MoO_2$ nanorod.*

X-ray photoelectron spectroscopy (XPS) was performed on the $MoNi_4/MoO_2$ as well as on the $MoS_2$:$MoNi_4/MoO_2$ hybrid to confirm the various ionic and electronic states of the elements, which provides further emphasis on the mechanism of the formation of the hybrid structure and its performances as electrocatalyst for HER. Figure 4.8a shows the comparative Mo 3d XPS peak from $MoNi_4/MoO_2$ and $MoS_2$:$MoNi_4/MoO_2$ (top) samples. Deconvolution of the Mo 3d peak from the $MoNi_4/MoO_2$ sample delineates individual peaks at 227.85 eV, 229.39 eV, 230.35 eV, and 232.43 eV emerge due to different valance states of $Mo^0$, $Mo^{4+}$, $Mo^{5+}$, and $Mo^{6+}$, respectively [34, 35]. Similarly, in hybrid $MoS_2$:$MoNi_4/MoO_2$ samples, the characteristics Mo 3d peak exhibited with 229.52 eV indicating the $Mo^{4+}$ oxidation state and

two corresponding peaks at 232.67 eV and 235.93 eV, representing the $Mo^{6+}$ oxidation state. Also, a $Mo^0$ peak is obtained along with the S 2s peak at their respective positions of 227.32 eV and 226.64 eV [32, 36, 37]. Additionally, Figure 4.8b demonstrates the comparative XPS peak of Ni 2p both in $MoNi_4/MoO_2$ and hybrid $MoS_2$:$MoNi_4/MoO_2$. For the $MoNi_4/MoO_2$ sample, the peak at 852.62 eV (Figure 4.8b) corresponds to the $Ni^0$, while other peaks at 855.98 eV and 873.62 eV are attributed to the $Ni^{2+}$ oxidation state [34, 38, 39]. For $MoS_2$:$MoNi_4/MoO_2$ hybrid material (Figure 4.8b), the characteristic peak positions of Ni 2p were found at 850.86 eV and 854.61 eV, which attributed to the oxidation states of $Ni^0$ and $Ni^{2+}$, respectively. Figure 4.8c shows the O1s spectrum in $MoNi_4/MoO_2$ at 530.49 eV, which is the characteristic of Mo–O species in $MoO_2$, while the other peak at 532.98 eV is attributed to the H–O bond of surface absorption species at oxygen vacancies [35, 40]. Furthermore, Figure 4.8d shows the characteristics S 2p peak appeared only in the hybrid $MoS_2$:$MoNi_4/MoO_2$, and the respective peak positions at 162.35 eV and 163.53 eV are associated with the $2p_{3/2}$ and $2p_{1/2}$ spin-orbit doublets indicating the $S^{2-}$ oxidation state of sulfur from $MoS_2$ [41, 42]. From the above XPS analysis, it is evident that the $Mo^0$, and $Mo^{4+}$ oxidation states refer to the successful formation of $MoNi_4$ and $MoO_2$ in a solid solution where the intermetallic $MoNi_4$ gets phase-separated in the $MoO_2$ matrix for both the samples of $MoNi_4/MoO_2$ and $MoS_2$:$MoNi_4/MoO_2$ [34]. The presence of $Ni^0$ oxidation state implies the formation of $MoNi_4$ in both the samples, while the appearance of Mo–O in the O 1s justifies the formation of $MoO_2$ in the composite nanorod. Similarly, the S 2s peaks and Mo oxidation states in $MoS_2$:$MoNi_4/MoO_2$ further validates the successful growth of $MoS_2$ on the $MoNi_4/MoO_2$ surface.

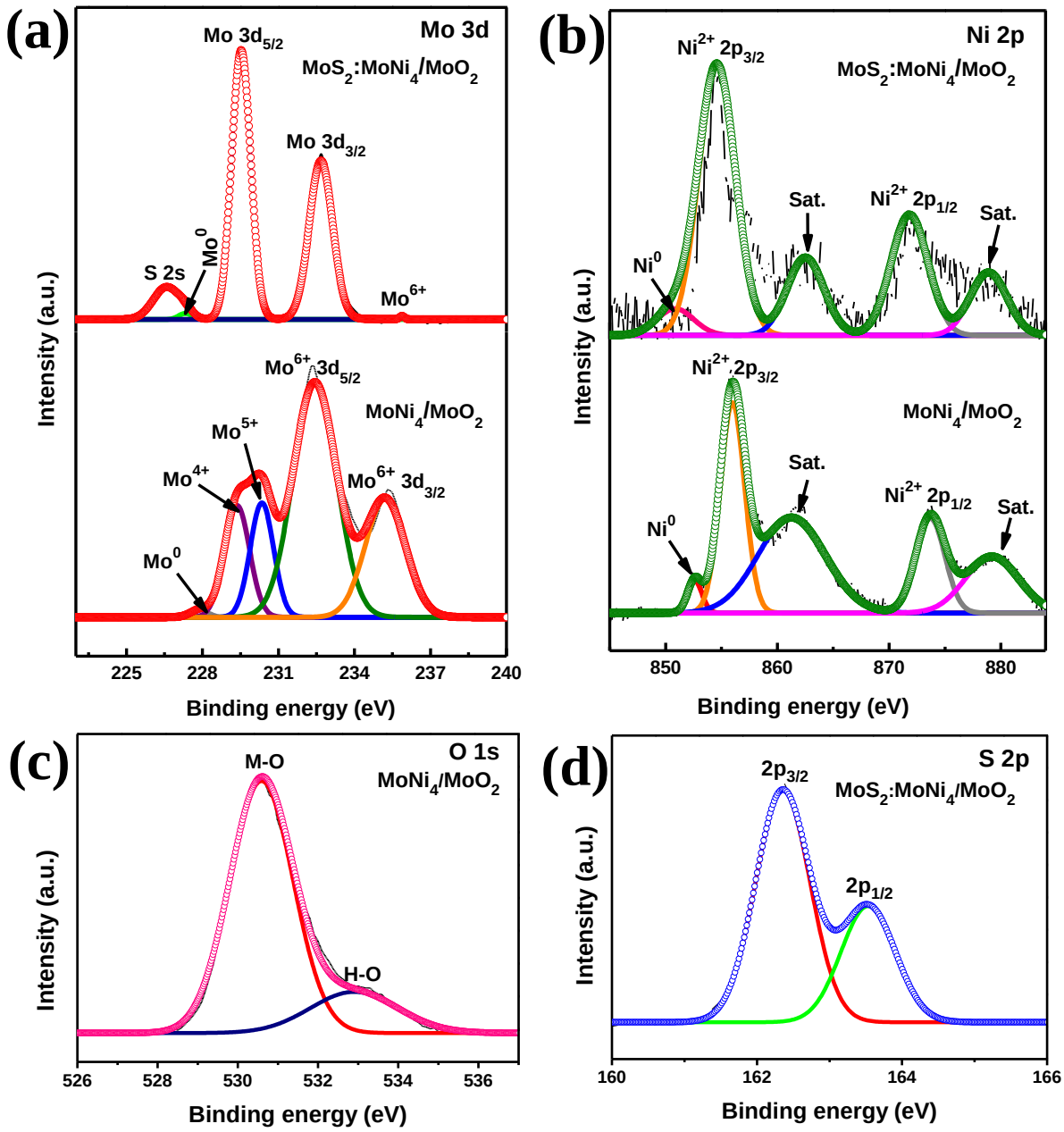


***Figure 4.8:*** *Shows the comparative (a) Mo 3d peaks, (b) Ni 2p peaks obtained from X-ray photoelectron spectroscopy of $MoNi_4/MoO_2$ and $MoS_2$:$MoNi_4/MoO_2$ hybrid; (c) and (d) illustrates O 1s peak from $MoNi_4/MoO_2$ sample and S 2p peak from the hybrid sample, respectively.*

For electrochemical studies all the electrodes were fabricated by drop-casting the as-synthesized nanohybrid powder as mentioned above after dispersing them in isopropanol

stabilized with Nafion solution on graphite paper with the effective area of 1 $cm^2$. Dispersions were prepared by adding 2.5 mg of the catalyst and 2.5 mg Vulcan XC72 Carbon powder in a 1060 µL solution prepared by adding 60 µL 5% Nafion, 500 µL isopropanol, 500 µL DI water, and sonicated for 40 min to form a homogeneous ink. 1060 µL dispersion was drop-casted on the graphite paper in multiple steps of 30 µL followed by drying in ambient conditions. Electrochemical characterization parameters were followed by section 2.3 of chapter 2.

The comparative electrocatalytic HER performances of all the catalysts were evaluated from the potentiodynamic polarization plots, as demonstrated in Figure 4.9a. A platinum (Pt) metal electrode was used as a benchmark catalyst, which shows onset potential (defined as potential at which current density of ~5 $mA/cm^2$ is achieved) of ~ 4 mV (vs. RHE), which represents comparatively high-catalytic activity as apparent from its current density values. We used graphite paper (GP) as a substrate for all the electrochemical characterizations, and we measured all the electrochemical parameters of GP itself under identical conditions. After adding dispersed $MoS_2$ on GP, the electrode showed better HER activity than the base graphite-paper substrate, showing the overpotential ( $\eta_5$) 191.5 mV (vs. RHE). This slower kinetics of the HER activity may be ascribed to weak adherence and the semiconducting behavior of the $MoS_2$. Similarly, $MoNi_4/MoO_2$ based electrode shows overpotential ($\eta_5$) 81.8 mV (vs. RHE). Low overpotential ($\eta_5$) was observed in $MoNi_4/MoO_2$ electrocatalyst due to its metallic behavior. For $MoS_2$:$MoNi_4/MoO_2$ nanohybrid, the overpotential ($\eta_5$) decreases significantly to 115.6 mV (vs. RHE), compared to the pristine $MoS_2$. Likewise, $\eta_{10}$ (as potential at which current density of ~10 $mA/cm^2$ is achieved) values for $MoS_2$ $MoNi_4/MoO_2$, and $MoS_2$:$MoNi_4/MoO_2$ were found to be 226.7 mV, 147.0 mV, and 155.6 mV, respectively, indicating the identical trends in the HER activities as listed in Table 4.1. The HER kinetics are accelerated with the presence of $MoNi_4/MoO_2$ nanorod, which provides a better-

conducting channel of electron transfer compared to the pristine $MoS_2$ in $MoS_2$:$MoNi_4/MoO_2$ nanohybrid electrocatalyst. Table 4.1 demonstrates the comparable as-obtained electrochemical parameters of $MoS_2$, $MoNi_4/MoO_2$, and $MoS_2$:$MoNi_4/MoO_2$ nanohybrids electrocatalysts.

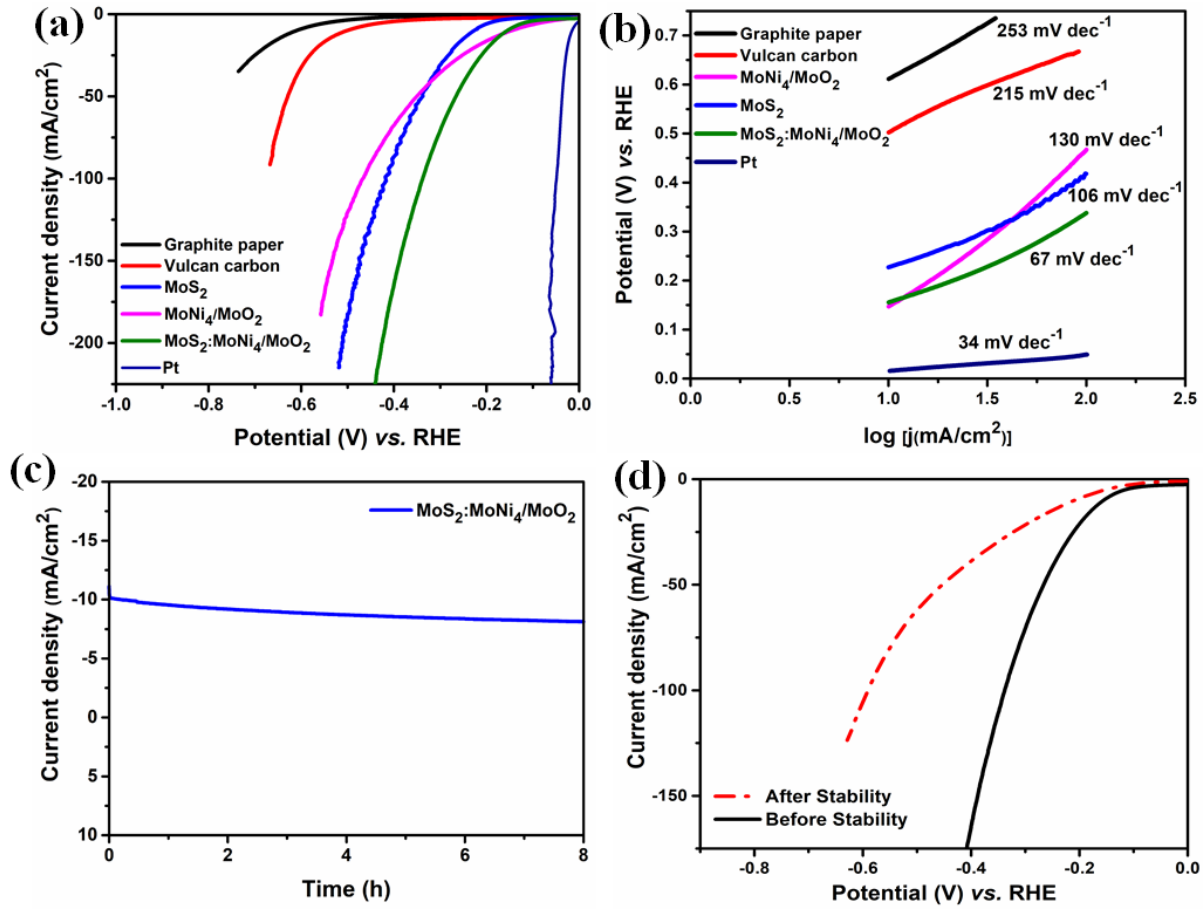


***Figure 4.9:*** *Illustrates (a) the comparative LSV plot of current density versus potential curve showing the onset potential for the hydrogen generation for all samples; (b) the correlative Tafel slopes for all samples; (c) the stability test of as-grown hybrid $MoS_2$:$MoNi_4/MoO_2$ electrocatalysts at constant overpotential at 200 mV; (d) A comparable linear sweep voltammetry (LSV) plot depicting the performance of the hybrid electrode before and after the stability test.*

**Table 4.1:** Lists the comparative electrochemical performances of $MoS_2$, $MoNi_4/MoO_2$ and $MoS_2$:$MoNi_4/MoO_2$ nanohybrids electrocatalysts

| Sample | $\eta_5$ (mV) | $\eta_{10}$ (mV) | β (mV $dec^{-1}$) | No of active sites (n) | $C_{dl}$ ($mF/cm^2$) | ECSA ($cm^2$) |
|---|---|---|---|---|---|---|
| Graphite paper | 541.6 | 610.8 | 253 | - | - | - |
| Vulcan carbon | 420.5 | 501.6 | 215 | - | - | - |
| $MoS_2$ | 191.5 | 226.7 | 106 | 2.832E14 | 0.0932 | 2970 |
| $MoNi_4/MoO_2$ | 81.8 | 147.0 | 130 | 3.087E14 | 0.0555 | 2725 |
| $MoS_2$:$MoNi_4/MoO_2$ | 115.6 | 155.6 | 67.0 | 4.694E14 | 0.1002 | 3200 |
| Pt | 3.8 | 19.2 | 34.0 | - | - | - |

The correlative Tafel plots in Figure 4.9b further manifest the enhancement of the kinetics of HER reaction of the $MoS_2$:$MoNi_4/MoO_2$ hybrid materials where Pt shows characteristic of single-electron Tafel step dependent process as Volmer step is very fast (Tafel slope of 34 $mVdec^{-1}$). Correspondingly, graphite paper, Vulcan carbon, $MoNi_4/MoO_2$, $MoS_2$, and $MoS_2$:$MoNi_4/MoO_2$ hybrid electrocatalysts show Tafel slopes of 253 $mVdec^{-1}$, 215 $mVdec^{-1}$, 130 $mVdec^{-1}$, 106 $mVdec^{-1}$, and 67 $mVdec^{-1}$, respectively. Among these as-synthesized electrocatalysts, the hybrid material-based electrodes exhibit the smaller Tafel slope, suggesting that a coupled Volmer-Heyrovsky type mechanism is followed for the HER. Specifically, it is evident that the Volmer step is predominant as the process involves electron transfer mechanisms while 2 electron processes are involved during the HER reaction as discussed in chapter 1 (section 1.3.1) follows [43-45].

Long-term electrocatalytic stability is one of the essential criteria to evaluate the performance of HER. Figure 4.9c shows the chronoamperometric (i-t) data of hybrid $MoS_2$:$MoNi_4$/$MoO_2$ electrocatalyst at a constant overpotential 200 mV (vs. RHE) for more than 8 h with the fixed current density of 10 mA/cm$^2$ in 1M KOH solution. We observed the lower current density from 10 mA/cm$^2$ to 8.11 mA/cm$^2$ after more than eight (8) hours of stability test [32, 46]. We used graphite paper as a substrate and graphite rod as a counter electrode for the electrochemical measurements of HER. The graphite counter electrode undergoes oxidation, at a thermodynamic potential of 0.2V (vs. RHE), during the HER of the studied catalyst, as reported earlier. The localized $CO_2$ production and functionalization of carbon surface result in increasing surface roughness and decreasing the electrode's electrical conductivity. Similarly, it is also justified that using carbon fiber paper (CFP) as a counter electrode, there is an extensive deterioration of the Pt mesh, working electrode, due to blockage of the catalyst's active sites [47]. We believe that the same phenomena happened during the experimentation of $MoS_2$:$MoNi_4$/$MoO_2$ during the stability test, which resulted in an increment in overpotential. Figure 4.9d illustrates comparative linear sweep voltammetry (LSV) data of the hybrid electrode (before the stability test and after the stability test) to demonstrate its reliability performance. It could be seen from Figure 4.9d that the overpotential of the hybrid electrode increased from 155 mV (vs. RHE) to 209 mV (vs. RHE) after the eight (8) hour stability test at a current density of 10 mA/cm$^2$.

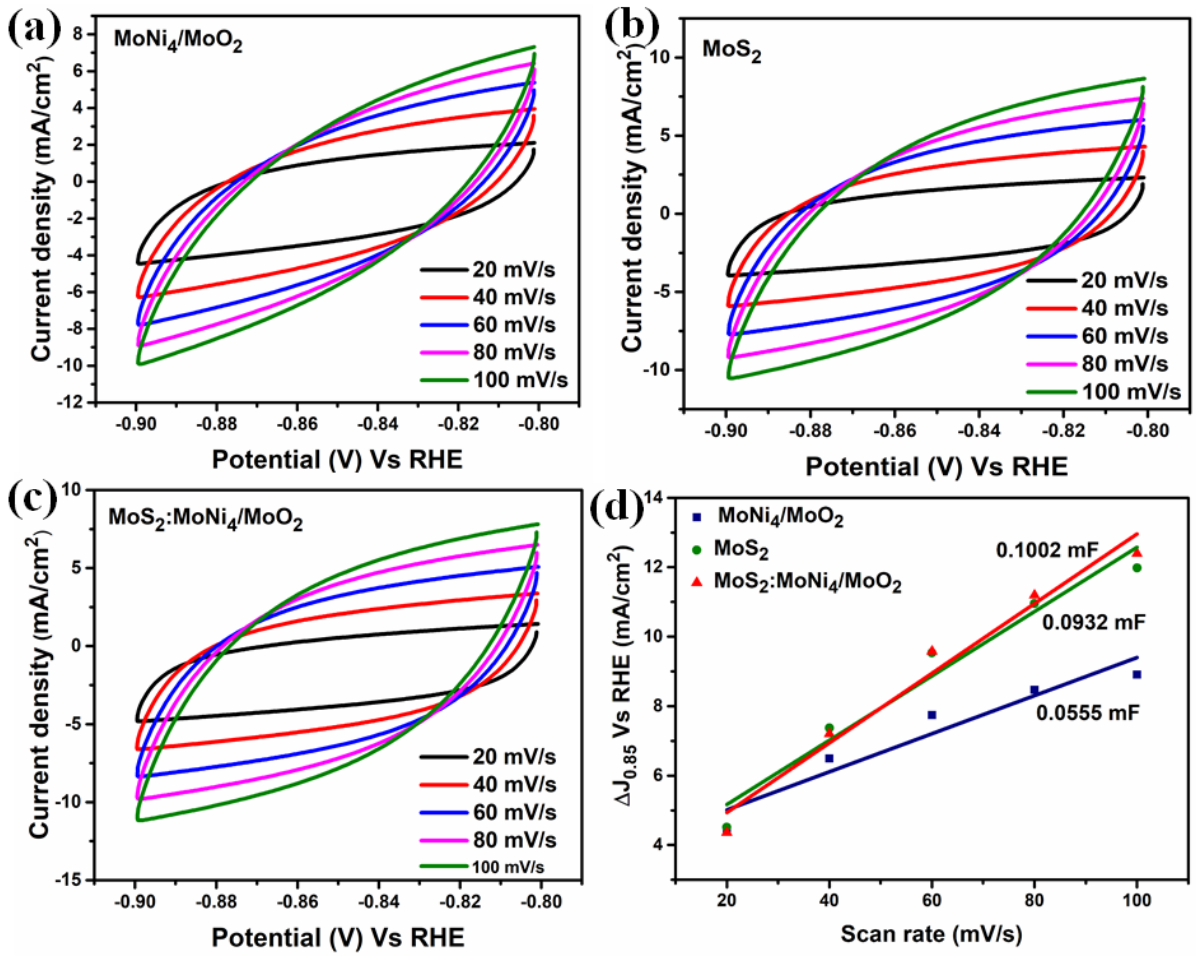


***Figure 4.10:*** *(a-c) Shows the cyclic voltammetry (CV) with different scan rates of 20-100 mV/s for $MoNi_4/MoO_2$ nanorod, $MoS_2$, and $MoS_2$:$MoNi_4/MoO_2$ nanohybrids. (d) Comparative $C_{dl}$ plot as a function of scan rate.*

Figure 4.10 (a-c) shows the cyclic voltammetry (CV) with different scan rates of 20-100 mV/s for $MoNi_4/MoO_2$ nanorod, $MoS_2$, and $MoS_2$:$MoNi_4/MoO_2$ nanohybrids. Figure 4.10d shows a comparative plot of electrochemical double-layer capacitance ($C_{dl}$) as a function of scan rate, which depicts the electrochemical surface area (ECSA) of all of the samples. The plot demonstrates the increase of the double-layer capacitance of the hybrid catalyst compared to the pristine $MoS_2$ and the $MoNi_4/MoO_2$ nanorod catalysts. The increase in the double-layer capacitance of hybrid material is further attributed to the increase in specific surface area and active sites of the charge transfer, as listed in Table 4.1. The detailed scan-

rate-dependent CV plot for electrochemical surface area (ECSA) calculations and the CV plot for the number of active sites calculations are shown in Figures 4.10 a-c and Figure 4.11, respectively.

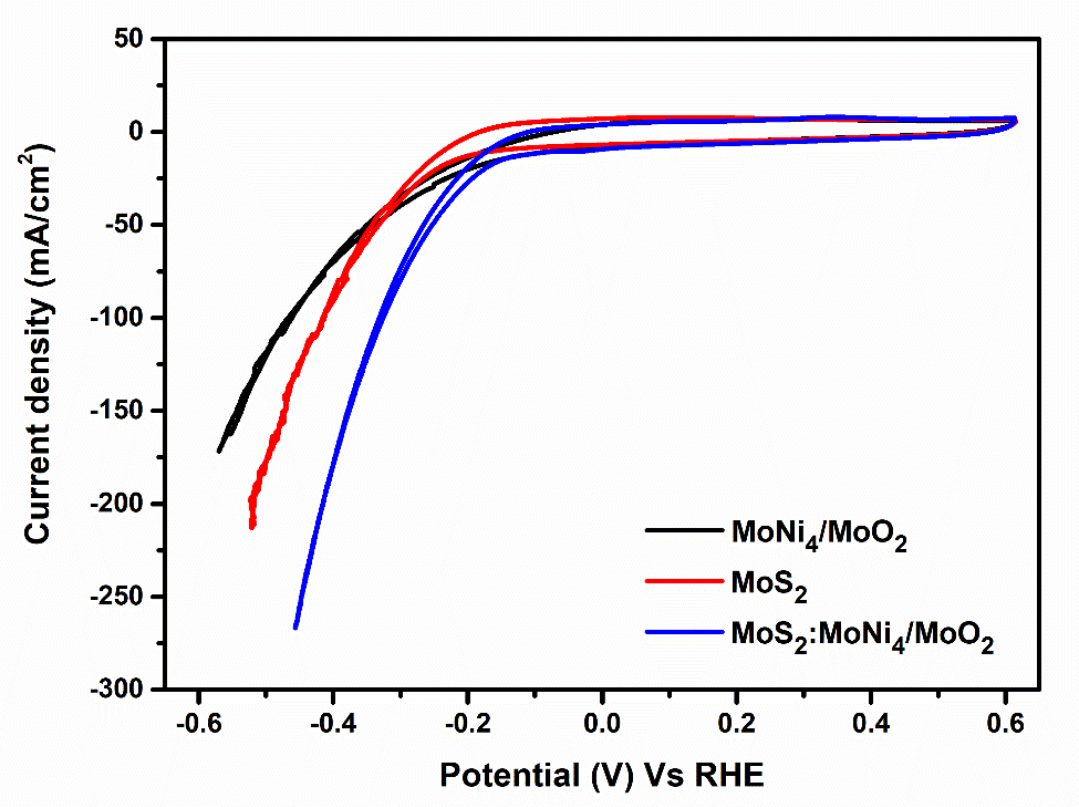


***Figure 4.11:*** *Comparative cyclic voltammetry curves of $MoNi_4/MoO_2$, $MoS_2$, and $MoS_2$:$MoNi_4/MoO_2$ hybrid structure recorded between -0.6 V to 0.6 V vs. RHE in 1M KOH at a scan rate of 20 mV/s.*

Since the difficulty in attributing the observed peaks to a given redox couple, the number of active sites should be proportional to the integrated charge over the cyclic voltammetry curve. So, let's assume a single electron process for oxidation and reduction. The number of active sites (n) for $MoS_2$, $MoNi_4/MoO_2$, and $MoS_2$:$MoNi_4/MoO_2$ nanohybrid is calculated according to the following Equation (4.1):

$$n = \frac{Q}{2F} \qquad (4.1)$$

Where n is the number of active sites, Q is the charges of the cyclic voltammetry curve, and F is the Faraday constant, respectively.

The HER kinetics at the electrode/electrolyte interface for the as-prepared electrocatalysts are investigated by electrochemical impedance spectroscopy (EIS) at -0.27 V vs. RHE. The EIS data of the $MoS_2$:$MoNi_4/MoO_2$, $MoS_2$, and $MoNi_4/MoO_2$ electrocatalysts are shown in Figure 4.12. The Randles equivalent circuit is used for fitting the EIS experimental results of $MoS_2$:$MoNi_4/MoO_2$, as shown in the inset of Figure 4.12. In the Randles circuit, the capacitor was replaced with a constant phase element (CPE), a typical characteristic of a coated thin-film electrode, representing the electrode behavior as a non-ideal/leaky capacitor. Simultaneously, $R_{ct}$ represents the charge transfer resistance, $R_s$ is the solution resistance, and $R_p$ is the adsorption resistance. The corresponding values of $R_{ct}$, $R_s$, and $R_p$ are obtained from the Randles circuit, as listed in Table 4.2. [48] The $MoS_2$:$MoNi_4/MoO_2$ hybrid catalyst shows a much smaller charge transfer resistance ($R_{ct}$) and solution resistance ($R_s$) compared with $MoS_2$ and $MoNi_4/MoO_2$, indicating the higher conductivity of the $MoS_2$:$MoNi_4/MoO_2$ hybrid catalyst. This is primarily due to a conducting channel of $MoNi_4/MoO_2$, suggesting better electron conductivity of $MoS_2$:$MoNi_4/MoO_2$ and more accessible charge transfer at the electrode/electrolyte interface, which is favorable for the electrocatalytic reaction. We also calculated the ECSA from the $CPE_2$ values obtained from the Randles circuit fitting of the Nyquist plot (Figure 4.12). As discussed in the previous section of this manuscript, the as calculated ECSA for all of the samples shows that the increase in the surface area of hybrid materials is equivalent, thereby increasing the HER kinetics.

$CPE_2$ is the capacitance contribution coming from the adsorption from the hybrid electrode surface. Therefore, we believe that, ideally, $CPE_2$ is the better indicator of electrochemical ECSA and the specific capacitance, which can be calculated by the following equations as follows:

$$Capacitance\ (C_{dl}) = \frac{(CPE_2 \text{ x } R_p)^{1/n}}{R_p} \quad (4.2)$$

$$ECSA = \frac{C_{dl}}{Specific\ \ capacitance} \quad (4.3)$$

The $CPE_2$ and $R_p$ values are obtained from the fitting of the Nyquist plot as given in Figure 7b, and the specific capacitance is considered as 0.04 mF/cm$^2$. From Table 4.1 the corresponding ECSA values (calculated from the $CPE_2$ values) are indicative of the successive increment of the surface area for the $MoS_2$:$MoNi_4/MoO_2$ hybrid material compared to the $MoS_2$ and $MoNi_4/MoO_2$ nanorod.

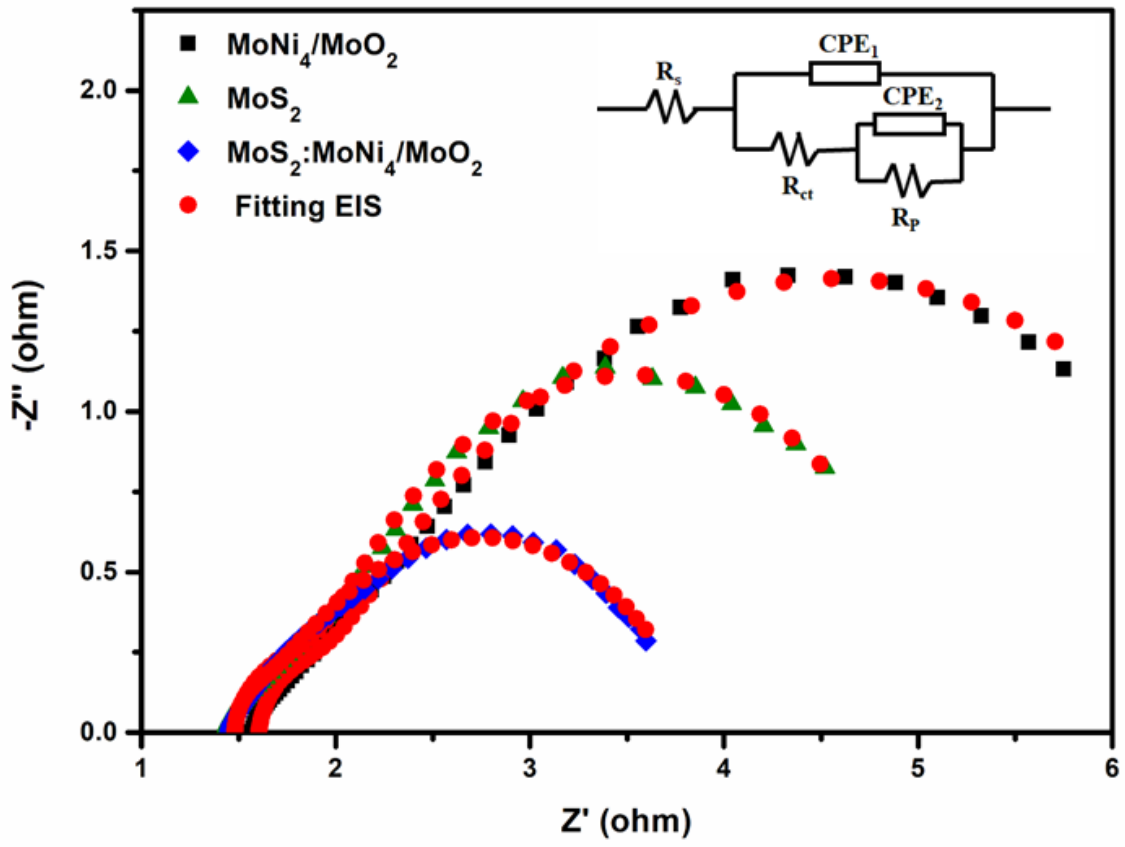


***Figure 4.12:*** *Comparable EIS data for pristine $MoS_2$, $MoNi_4/MoO_2$, and $MoS_2$:$MoNi_4/MoO_2$ hybrid sample.*

**Table 4.2:** Lists the fitting parameters from the EIS equnvalent circuit model

| Parameter | $MoS_2$:$MoNi_4/MoO_2$ | $MoS_2$ | $MoNi_4/MoO_2$ |
|---|---|---|---|
| $R_s$ (Ω) | 1.10 | 1.44 | 1.60 |
| $CPE_1$ (S-sec$^n$) | 0.0039 | 0.027 | 0.0038 |
| $n_1$ | 1 | 0.7635 | 0.919 |
| $R_{ct}$ (Ω) | 0.2403 | 0.6221 | 3.493 |
| $CPE_2$ (S-sec$^n$) | 0.1766 | 0.1543 | 0.1243 |
| $n_2$ | 0.75 | 0.75 | 0.75 |
| $R_p$ (Ω) | 2.172 | 2.961 | 5.425 |

**Table 4.3:** The comparative HER performances of $MoS_2$:$MoNi_4/MoO_2$ nanohybrid with various other $MoS_2$-based hybrid electrocatalysts reported to date.

| Catalysts | Overpotential (mV, 10 mA cm$^{-2}$) | Tafel slop (mV/dec) | Electrolyte | References |
|---|---|---|---|---|
| $MoS_2$:$MoNi_4/MoO_2$ | 155.6 | 67 | 1M KOH | This work |
| 2H-$MoS_2$ | 226.7 | 106 | 1M KOH | This work |
| $MoNi_4/MoO_2$ | 147 | 130 | 1M KOH | This work |
| Bulk $MoS_2$ | 578 | 143 | 0.5M $H_2SO_4$ | [49] |
| 2H-$MoS_2$ | 229 | 109 | 1M KOH | [50] |
| 3R-$MoS_2$ | 520 | 113 | 0.5M $H_2SO_4$ | [51] |
| 1T-$MoS_2$ | 111 | 53 | 0.5M $H_2SO_4$ | [52] |
| 1T′-$MoS_2$ | 300 | 83 | 0.5M $H_2SO_4$ | [53] |
| 1T-$MoS_2$ | 100 | 40 | 0.5M $H_2SO_4$ | [54] |
| Ultrathin $MoS_2$ NP* | - | 53 | 0.5M $H_2SO_4$ | [55] |
| Defect Rich $MoS_2$ | 70 | 50 | 0.5M $H_2SO_4$ | [22] |

*(NP: Nanoplates)

Overall, it is quite evident that the $MoS_2$:$MoNi_4$/$MoO_2$ hybrids exhibit a unique and versatile structure showing excellent catalytic activities for HER reactions. Our claim is also noticeable from the comparative performances of $MoS_2$:$MoNi_4$/$MoO_2$ hybrid material with earlier reported $MoS_2$ based electrocatalysts, as listed in Table 4.3. The synergistic hybrid nanostructures containing the flaky $MoS_2$ grown on $MoNi_4$/$MoO_2$ nanorods primarily enlarge the hybrids' specific surface area. Furthermore, the nano-heterostructure exhibits various synergistically assembled catalytically active phases, like $MoNi_4$ and $MoS_2$ (2D) connected to a conducting $MoO_2$ (1D) nanorod, which principally enhances the surface area, thereby improving the charge-transport kinetics for HER. Thus, we believe this work will pave a pathway toward further development in producing other 1D/2D/3D-materials-based hybrid electrodes in various electrochemical energy devices.

### 4.3 Chapter summary

In summary, we have developed a synergistic hierarchical structure consisting of bulk $MoNi_4$/$MoO_2$ nanorods coated with vertically aligned 2D $MoS_2$ flakes for hydrogen evolution reaction. We used a hydrothermal method for synthesis where we obtained that $MoNi_4$/$MoO_2$ nanorod assembled with 2D flaky $MoS_2$ simultaneously improved the interfacial charge transport properties of the hybrid $MoS_2$:$MoNi_4$/$MoO_2$ structures, thus, acting as an active catalyst for enhanced HER. The as-grown 2D $MoS_2$ is a vertically aligned forest-like structure grown via a self-limiting hydrothermal process. The $MoS_2$ flakes are developed like flower petals-shaped structures with a size of ~ 300-500 nm and thickness of ~ 2-5 nm. Numerous structural characterizations, such as XRD, FESEM, TEM/HRTEM, and XPS, show that the synergistic nanohybrid structure forms with high surface area and distinct electrocatalytically active phases. As a growth mechanism of the formation of the nanohybrid structure, we found that initially, sulfur super-saturation occurred in the aqueous solution under elevated

temperature and pressure, followed by the catalytic growth of 2D flaky $MoS_2$. We also obtained the formation of various active surface species, which we believe play a key role in enhancing the catalytic activities of vertically aligned $MoS_2$ on the surface of the nanorods. The electrochemical results demonstrate the extraordinary improvements in the performance of HER reaction of the nanohybrids compared to the pristine $MoS_2$ by lowering the overpotential, increasing the surface area, and enhancing the interfacial charge transfer kinetics. We further believe that this work will open a new research field and be applicable to other energy-harvesting and storage devices, including solar cells, batteries, fuel cells, supercapacitors, and many more.

**References**


[1] J. Deng, P. Ren, D. Deng, L. Yu, F. Yang, and X. Bao, "Highly active and durable non-precious-metal catalysts encapsulated in carbon nanotubes for hydrogen evolution reaction," *Energy & Environmental Science,* vol. 7, no. 6, pp. 1919-1923, 2014, doi: 10.1039/C4EE00370E.

[2] H. B. Wu, B. Y. Xia, L. Yu, X.-Y. Yu, and X. W. Lou, "Porous molybdenum carbide nano-octahedrons synthesized via confined carburization in metal-organic frameworks for efficient hydrogen production," *Nature Communications,* Article vol. 6, p. 6512, 2015, doi: 10.1038/ncomms7512.

[3] J. McAllister *et al.*, "Tuning and mechanistic insights of metal chalcogenide molecular catalysts for the hydrogen-evolution reaction," *Nature Communications,* vol. 10, no. 1, p. 370, 2019, doi: 10.1038/s41467-018-08208-4.

[4] H. Yan *et al.*, "Phosphorus-Modified Tungsten Nitride/Reduced Graphene Oxide as a High-Performance, Non-Noble-Metal Electrocatalyst for the Hydrogen Evolution Reaction," *Angewandte Chemie International Edition,* vol. 54, no. 21, pp. 6325-6329, 2015, doi: 10.1002/anie.201501419.

[5] C. Tang *et al.*, "Fe-Doped CoP Nanoarray: A Monolithic Multifunctional Catalyst for Highly Efficient Hydrogen Generation," *Advanced Materials,* vol. 29, no. 2, p. 1602441, 2017, doi: https://doi.org/10.1002/adma.201602441.

[6] X. Fan, Z. Peng, J. Wang, R. Ye, H. Zhou, and X. Guo, "Carbon-Based Composite as an Efficient and Stable Metal-Free Electrocatalyst," *Advanced Functional Materials,* vol. 26, no. 21, pp. 3621-3629, 2016, doi: https://doi.org/10.1002/adfm.201600076.

[7] Y. Zheng *et al.*, "Hydrogen evolution by a metal-free electrocatalyst," *Nature Communications,* Article vol. 5, p. 3783, 2014, doi: 10.1038/ncomms4783.

[8] M. Xia, T. Lei, N. Lv, and N. Li, "Synthesis and electrocatalytic hydrogen evolution performance of Ni–Mo–Cu alloy coating electrode," *International Journal of Hydrogen Energy,* vol. 39, no. 10, pp. 4794-4802, 2014.

[9] R. Subbaraman *et al.*, "Trends in activity for the water electrolyser reactions on 3d M(Ni,Co,Fe,Mn) hydr(oxy)oxide catalysts," *Nature Materials,* Article vol. 11, p. 550, 2012, doi: 10.1038/nmat3313.

[10] S. Badrayyana, D. K. Bhat, S. Shenoy, Y. Ullal, and A. C. Hegde, "Novel Fe–Ni-Graphene composite electrode for hydrogen production," *International Journal of Hydrogen Energy,* vol. 40, no. 33, pp. 10453-10462, 2015.

[11] J. Zhang *et al.*, "Efficient hydrogen production on $MoNi_4$ electrocatalysts with fast water dissociation kinetics," *Nature Communications,* Article vol. 8, p. 15437, 2017, doi: 10.1038/ncomms15437.

[12] P. D. Tran *et al.*, "Coordination polymer structure and revisited hydrogen evolution catalytic mechanism for amorphous molybdenum sulfide," *Nature Materials,* Article vol. 15, p. 640, 2016, doi: 10.1038/nmat4588.

[13] J. W. D. Ng *et al.*, "Gold-supported cerium-doped $NiO_x$ catalysts for water oxidation," *Nature Energy,* Article vol. 1, p. 16053, 2016, doi: 10.1038/nenergy.2016.53.

[14] J. Staszak-Jirkovský *et al.*, "Design of active and stable Co–Mo–$S_x$ chalcogels as pH-universal catalysts for the hydrogen evolution reaction," *Nature Materials,* Article vol. 15, p. 197, 2015, doi: 10.1038/nmat4481.

[15] Z. Chen, X. Duan, W. Wei, S. Wang, and B.-J. Ni, "Recent advances in transition metal-based electrocatalysts for alkaline hydrogen evolution," *Journal of Materials Chemistry A,* vol. 7, no. 25, pp. 14971-15005, 2019, doi: 10.1039/C9TA03220G.

[16] Y. Wang, D. Yan, S. El Hankari, Y. Zou, and S. Wang, "Recent Progress on Layered Double Hydroxides and Their Derivatives for Electrocatalytic Water Splitting," *Advanced Science,* vol. 5, no. 8, p. 1800064, 2018.

[17] R. Zhang *et al.*, "Ternary $NiCo_2P_x$ Nanowires as pH-Universal Electrocatalysts for Highly Efficient Hydrogen Evolution Reaction," *Advanced Materials,* vol. 29, no. 9, p. 1605502, 2017, doi: 10.1002/adma.201605502.

[18] H. Wang, C. Li, P. Fang, Z. Zhang, and J. Z. Zhang, "Synthesis, properties, and optoelectronic applications of two-dimensional $MoS_2$ and $MoS_2$-based heterostructures," *Chemical Society Reviews,* vol. 47, no. 16, pp. 6101-6127, 2018, doi: 10.1039/C8CS00314A.

[19] H. Wang *et al.*, "High Electrochemical Selectivity of Edge versus Terrace Sites in Two-Dimensional Layered $MoS_2$ Materials," *Nano Letters,* vol. 14, no. 12, pp. 7138-7144, 2014, doi: 10.1021/nl503730c.

[20] Q. Wei *et al.*, "Directionally assembled $MoS_2$ with significantly expanded interlayer spacing: a superior anode material for high-rate lithium-ion batteries," *Materials Chemistry Frontiers,* vol. 2, no. 8, pp. 1441-1448, 2018, doi: 10.1039/C8QM00117K.

[21] J. Xie *et al.*, "Controllable Disorder Engineering in Oxygen-Incorporated $MoS_2$ Ultrathin Nanosheets for Efficient Hydrogen Evolution," *Journal of the American Chemical Society,* vol. 135, no. 47, pp. 17881-17888, 2013, doi: 10.1021/ja408329q.

[22] J. Xie *et al.*, "Defect-Rich $Mo_{S2}$ Ultrathin Nanosheets with Additional Active Edge Sites for Enhanced Electrocatalytic Hydrogen Evolution," *Advanced Materials,* vol. 25, no. 40, pp. 5807-5813, 2013, doi: 10.1002/adma.201302685.

[23] Y. Ouyang, C. Ling, Q. Chen, Z. Wang, L. Shi, and J. Wang, "Activating Inert Basal Planes of $MoS_2$ for Hydrogen Evolution Reaction through the Formation of Different Intrinsic Defects," *Chemistry of Materials,* vol. 28, no. 12, pp. 4390-4396, 2016, doi: 10.1021/acs.chemmater.6b01395.

[24] Y. Kim *et al.*, "In Situ Electrochemical Activation of Atomic Layer Deposition Coated $MoS_2$ Basal Planes for Efficient Hydrogen Evolution Reaction," *Advanced Functional Materials,* vol. 27, no. 34, p. 1701825, 2017, doi: 10.1002/adfm.201701825.

[25] X. Dai *et al.*, "Co-Doped $MoS_2$ Nanosheets with the Dominant CoMoS Phase Coated on Carbon as an Excellent Electrocatalyst for Hydrogen Evolution," *ACS Applied Materials & Interfaces,* vol. 7, no. 49, pp. 27242-27253, 2015, doi: 10.1021/acsami.5b08420.

[26] X. Yin *et al.*, "Quasi-Emulsion Confined Synthesis of Edge-Rich Ultrathin $MoS_2$ Nanosheets/Graphene Hybrid for Enhanced Hydrogen Evolution," *Chemistry – A European Journal,* vol. 24, no. 3, pp. 556-560, 2018, doi: 10.1002/chem.201703493.

[27] C. Bara *et al.*, "Aqueous-Phase Preparation of Model HDS Catalysts on Planar Alumina Substrates: Support Effect on Mo Adsorption and Sulfidation," *Journal of the American Chemical Society,* vol. 137, no. 50, pp. 15915-15928, 2015, doi: 10.1021/jacs.5b10975.

[28] M. N. McCain, B. He, J. Sanati, Q. J. Wang, and T. J. Marks, "Aerosol-Assisted Chemical Vapor Deposition of Lubricating $MoS_2$ Films. Ferrous Substrates and Titanium Film Doping," *Chemistry of Materials,* vol. 20, no. 16, pp. 5438-5443, 2008, doi: 10.1021/cm7026674.

[29] M. Vrinat, M. Breysse, C. Geantet, J. Ramirez, and F. Massoth, "Effect of $MoS_2$ morphology on the HDS activity of hydrotreating catalysts," *Catalysis Letters,* vol. 26, no. 1, pp. 25-35, 1994, doi: 10.1007/BF00824029.

[30] W. Zhou *et al.*, "Three-Dimensional Hierarchical Frameworks Based on $MoS_2$ Nanosheets Self-Assembled on Graphene Oxide for Efficient Electrocatalytic Hydrogen Evolution," *ACS Applied Materials & Interfaces,* vol. 6, no. 23, pp. 21534-21540, 2014, doi: 10.1021/am506545g.

[31] D. J. Li *et al.*, "Molybdenum Sulfide/N-Doped CNT Forest Hybrid Catalysts for High-Performance Hydrogen Evolution Reaction," *Nano Letters*, vol. 14, no. 3, pp. 1228-1233, 2014, doi: 10.1021/nl404108a.

[32] W. Li, Z. Zhang, W. Zhang, and S. Zou, "$MoS_2$ Nanosheets Supported on Hollow Carbon Spheres as Efficient Catalysts for Electrochemical Hydrogen Evolution Reaction," *ACS Omega*, vol. 2, no. 8, pp. 5087-5094, 2017, doi: 10.1021/acsomega.7b00755.

[33] Z. Xiang, Z. Zhang, X. Xu, Q. Zhang, and C. Yuan, "$MoS_2$ nanosheets array on carbon cloth as a 3D electrode for highly efficient electrochemical hydrogen evolution," *Carbon*, vol. 98, pp. 84-89, 2016.

[34] Y.-Y. Chen *et al.*, "Self-Templated Fabrication of $MoNi_4/MoO_{3-x}$ Nanorod Arrays with Dual Active Components for Highly Efficient Hydrogen Evolution," *Advanced Materials*, vol. 29, no. 39, p. 1703311, 2017.

[35] L. Meng *et al.*, "Valence-engineered $MoNi_4/MoO_x$@NF as a Bi-functional electrocatalyst compelling for urea-assisted water splitting reaction," *Electrochimica Acta*, vol. 350, p. 136382, 2020,

[36] J. Teich *et al.*, "Light and complex 3D $MoS_2$/graphene heterostructures as efficient catalysts for the hydrogen evolution reaction," *Nanoscale*, vol. 12, no. 4, pp. 2715-2725, 2020, doi: 10.1039/C9NR09564K.

[37] Y. Deng *et al.*, "Oxygen-incorporated MoX (X: S, Se or P) nanosheets via universal and controlled electrochemical anodic activation for enhanced hydrogen evolution activity," *Nano Energy*, vol. 62, pp. 338-347, 2019.

[38] S. A. Shah *et al.*, "Nickel@Nitrogen-Doped Carbon@$MoS_2$ Nanosheets: An Efficient Electrocatalyst for Hydrogen Evolution Reaction," *Small*, vol. 15, no. 9, p. 1804545,2019.

[39] L. Yang *et al.*, "Hierarchical microsphere of MoNi porous nanosheets as electrocatalyst and cocatalyst for hydrogen evolution reaction," *Applied Catalysis B: Environmental*, vol. 249, pp. 98-105, 2019.

[40] L. J. Yang, Y. Q. Deng, X. F. Zhang, H. Liu, and W. J. Zhou, "$MoSe_2$ nanosheet/$MoO_2$ nanobelt/carbon nanotube membrane as flexible and multifunctional electrodes for full water

splitting in acidic electrolyte," *Nanoscale,* vol. 10, no. 19, pp. 9268-9275, 2018, doi: 10.1039/C8NR01572D.

[41] K. Chang *et al.*, "Ultrathin $MoS_2$/Nitrogen-Doped Graphene Nanosheets with Highly Reversible Lithium Storage," *Advanced Energy Materials,* vol. 3, no. 7, pp. 839-844, 2013, doi: https://doi.org/10.1002/aenm.201201108.

[42] L. Yang *et al.*, "Hierarchical spheres constructed by defect-rich $MoS_2$/carbon nanosheets for efficient electrocatalytic hydrogen evolution," *Nano Energy,* vol. 22, pp. 490-498, 2016, doi: https://doi.org/10.1016/j.nanoen.2016.02.056.

[43] X. Lu, M. Cai, Z. Zou, J. Huang, and C. Xu, "A novel MoNi@$Ni(OH)_2$ heterostructure with Pt-like and stable electrocatalytic activity for the hydrogen evolution reaction," *Chemical Communications*, vol. 56, no. 11, pp. 1729-1732, 2020, doi: 10.1039/C9CC08985C.

[44] Y. Zheng, Y. Jiao, M. Jaroniec, and S. Z. Qiao, "Advancing the Electrochemistry of the Hydrogen-Evolution Reaction through Combining Experiment and Theory," *Angewandte Chemie International Edition,* vol. 54, no. 1, pp. 52-65, 2015.

[45] W. Fu *et al.*, "Surface-Electron Coupling for Efficient Hydrogen Evolution," *Angewandte Chemie International Edition*, vol. 58, no. 49, pp. 17709-17717, 2019, doi: 10.1002/anie.201908938.

[46] J. Ren *et al.*, "2D organ-like molybdenum carbide (MXene) coupled with $MoS_2$ nanoflowers enhances the catalytic activity in the hydrogen evolution reaction," *CrystEngComm*, vol. 22, no. 8, pp. 1395-1403, 2020, doi: 10.1039/C9CE01777A.

[47] J. Lee and J. H. Bang, "Reliable Counter Electrodes for the Hydrogen Evolution Reaction in Acidic Media," *ACS Energy Letters*, vol. 5, no. 8, pp. 2706-2710, 2020, doi: 10.1021/acsenergylett.0c01537.

[48] F. Li *et al.*, "$MoS_2$ quantum dot decorated RGO: a designed electrocatalyst with high active site density for the hydrogen evolution reaction," *Journal of Materials Chemistry A,* vol. 3, no. 43, pp. 21772-21778, 2015, doi: 10.1039/C5TA05219J.

[49] X. Lu *et al.*, "One-Step Hydrothermal Fabrication of Three-dimensional $MoS_2$ Nanoflower using Polypyrrole as Template for Efficient Hydrogen Evolution Reaction," *Scientific Reports*, vol. 7, no. 1, p. 42309, 2017, doi: 10.1038/srep42309.

[50] D. Zhu, J. Liu, Y. Zhao, Y. Zheng, and S.-Z. Qiao, "Engineering 2D Metal–Organic Framework/$MoS_2$ Interface for Enhanced Alkaline Hydrogen Evolution," *Small*, vol. 15, no. 14, p. 1805511, 2019, doi: https://doi.org/10.1002/smll.201805511.

[51] R. J. Toh, Z. Sofer, J. Luxa, D. Sedmidubský, and M. Pumera, "3R phase of $MoS_2$ and $WS_2$ outperforms the corresponding 2H phase for hydrogen evolution," *Chemical Communications*, vol. 53, no. 21, pp. 3054-3057, 2017, doi: 10.1039/C6CC09952A.

[52] K. Zhang *et al.*, "Aligned Heterointerface-Induced 1T-$MoS_2$ Monolayer with Near-Ideal Gibbs Free for Stable Hydrogen Evolution Reaction," *Small*, vol. 15, no. 8, p. 1804903, 2019, doi: https://doi.org/10.1002/smll.201804903.

[53] J. Zhang *et al.*, "Unveiling Active Sites for the Hydrogen Evolution Reaction on Monolayer $MoS_2$," *Advanced Materials*, vol. 29, no. 42, p. 1701955, 2017, doi: https://doi.org/10.1002/adma.201701955.

[54] D. Voiry *et al.*, "Conducting $MoS_2$ Nanosheets as Catalysts for Hydrogen Evolution Reaction," *Nano Letters*, vol. 13, no. 12, pp. 6222-6227, 2013, doi: 10.1021/nl403661s.

[55] Y. Yan, B. Xia, X. Ge, Z. Liu, J.-Y. Wang, and X. Wang, "Ultrathin $MoS_2$ Nanoplates with Rich Active Sites as Highly Efficient Catalyst for Hydrogen Evolution," *ACS Applied Materials & Interfaces*, vol. 5, no. 24, pp. 12794-12798, 2013, doi: 10.1021/am404843b.